Microstructure evolution and texture tailoring of reduced graphene oxide reinforced Zn scaffold

Youwen Yang [a], Yun Cheng [a], Shuping Peng [b,c], Liang Xu [c], Chongxian He [a], Fangwei Qi [a], Mingchun Zhao [d], Cijun Shuai [a,e,f,*]

[a] Institute of Bioadditive Manufacturing, Jiangxi University of Science and Technology, Nanchang, 330013, China
[b] NHC Key Laboratory of Carcinogenesis, School of Basic Medical Science, Central South University, Changsha, Hunan, 410013, China
[c] School of Energy and Machinery Engineering, Jiangxi University of Science and Technology, Nanchang, 330013, China
[d] School of Materials and Engineering, Central South University, Changsha, 410083, China
[e] State Key Laboratory of High Performance Complex Manufacturing, Central South University, Changsha, 410083, China
[f] Shenzhen Institute of Information Technology, Shenzhen, 518172, China

ARTICLE INFO

ABSTRACT

Zinc (Zn) possesses desirable degradability and favorable biocompatibility, thus being recognized as a promising bone implant material. Nevertheless, the insufficient mechanical performance limits its further clinical application. In this study, reduced graphene oxide (RGO) was used as reinforcement in Zn scaffold fabricated via laser additive manufacturing. Results showed that the homogeneously dispersed RGO simultaneously enhanced the strength and ductility of Zn scaffold. On one hand, the enhanced strength was ascribed to (i) the grain refinement caused by the pinning effect of RGO, (ii) the efficient load shift due to the huge specific surface area of RGO and the favorable interface bonding between RGO and Zn matrix, and (iii) the Orowan strengthening by the homogeneously distributed RGO. On the other hand, the improved ductility was owing to the RGO-induced random orientation of grain with texture index reducing from 20.5 to 7.3, which activated more slip systems and provided more space to accommodate dislocation. Furthermore, the cell test confirmed that RGO promoted cell growth and differentiation. This study demonstrated the great potential of RGO in tailoring the mechanical performance and cell behavior of Zn scaffold for bone repair.

1. Introduction

Biodegradable metals are recognized to be one new generation of bone repair material [1,2]. Among them, magnesium (Mg) alloy has been intensively investigated during the past decade [3,4]. Nevertheless, it exhibits too rapid a degradation because of its active chemical property, which usually causes a premature failure before bone healing. Iron (Fe) alloy has also been studied as temporary bone substitute, but it degrades too slowly and limits the new bone regeneration [5,6]. Recently, Zinc (Zn), one new type of biodegradable metal, has drawn intensive attention of researchers [7–9]. It possesses an intermediate standard potential (−0.76 V) between that of Mg (−2.37 V) and Fe (−0.44 V), which potentially has a more suitable degradation rate in clinical requirement [10]. Meanwhile, its degradation product can stimulate osteoblast formation and inhibit osteoclast differentiation [11]. Nevertheless, one issue deserves our concern is that Zn exhibits insufficient mechanical performances, which currently limits its further orthopedic application.

Introducing nano reinforcements, such as nanoparticle, nanorod and nanosheet, is an effective way to improve the mechanical properties of metal materials [12–14]. The possible strengthening mechanism mainly includes (i) grain refinement, (ii) load-transfer effect, (iii) Orowan strengthening, and (iv) thermal expansion differences between the matrix and reinforcements [15]. Among them, the load-transfer effect and grain refinement are usually recognized as the two major factors that have impacts on the strengthening [16]. Particularly, graphene nano sheets possess superior strength and elasticity modulus [17,18]. More significantly, they possess a huge aspect ratio. Thus, it is expected that the incorporated graphene nanosheets are able to cause an efficient loading transfer and accordingly contribute to a major strengthening effect. Xiang et al. [19] incorporated graphene nanoplatelets into Mg alloy, which significantly improved the tensile strength. Yue et al. [20]

---

added graphene nanosheets into copper matrix composite, which both enhanced the ultimate tensile strength and elongation. Li et al. [21] used reduced graphene oxide (RGO) to enhance TiAl alloy, which exhibited the superior compressive strength. Han et al. [22] fabricated RGO-reinforced Al alloy, which possessed considerably improved uni-axial yield and tensile strength. In addition, previous researches have also proved that graphene showed good biocompatibility and even exerted a positive role for cell growth and development [23].

In present study, RGO, one graphene derivative, was used as rein-forcement to prepare Zn-based scaffold via laser powder bed fusion (LPBF). As one additive manufacturing technology, LPBF exhibits a high flexibility and efficiency in producing parts with complex structure and customized shape [24–26]. On the other hand, it utilizes high-energy laser as heat source, which enable it can deal with a wide range of material system. Thus, it has been recognized as a preferable method to manufacture porous scaffold. The influence of RGO on the microstruc-ture including grain size, texture feature and dislocation density was investigated systematically. It was focused on the reinforcing mecha-nism of RGO on the mechanical performance of Zn scaffold. Further-more, the *in vitro* corrosion and cell response were studied aiming to evaluate the practicability of Zn-RGO scaffold for orthopedic application.

2. Material and methods

2.1. Preparation of RGO

The original graphene oxide (GO, purity>99.9%) was supplied by nano technology Co. Solvothermal reduction method was carried out to reduce the GO into RGO. Their chemical composition was examined by X-ray photoelectron spectroscopy (XPS, PHI5702, ULVCA-PHI, USA). Besides, the quality of RGO was further investigated using X-ray diffraction (XRD, D8 Advance, Bruker, Germany) and Raman spectros-copy (JY-HR800).

2.2. Laser additive manufacturing process

The RGO flakes had a diameter ranging from 0.3 to 2 μm, as showed in Fig. 1a. It could be seen that RGO exhibited typical wrinkled surface. The Zn powder produced by gas atomization technique was obtained from Nano Powder Co. (Shanghai, China), as showed in Fig. 1b. The D10 and D90 were 15 and 53 μm, respectively. The Zn powder and RGO (0.1 wt%, 0.2 wt%, 0.3 wt%, respectively) were homogeneously mixed using a ball mill at 200 rpm for 4 h, as exhibited in Fig. 1c. During milling, argon gas was supplied to prevent oxidation.

A LPBF system was adopted to prepare Zn and Zn-RGO scaffolds. It was consisted of a fiber laser (IPG YLR-500) with a spot size of 50 μm, automatic powder spreading system and a computer system for process control. A standard alternating *x/y* raster strategy which firstly scanned in *x*-direction and then shifted to *y*-direction in the next layer was uti-lized during LPBF. In order to obtain favorable forming quality, a series of pre-experiments were carried out to optimize the process. The optimal processing parameters were set as follows: laser power 80 W, scanning speed 550 mm/s, scanning distance 40 μm. During LPBF, a strict argon environment with oxygen content below 0.1 ppm was offered. The scaffold mode adopted in LPBF was exhibited in Fig. 1d. It possessed a porous structure with a designed strut thickness of 500 μm, and a porosity of 75.8%.

2.3. Microstructural characterizations

A scanning electron microscopy (SEM, EVO 18, Zeiss, Germany) was utilized to observe the surface of as-built scaffolds. The scaffold was then polished and further observed using SEM equipped with an energy dispersive spectroscopy (EDS, X-Max 20, Oxford instruments, UK).

The electron backscatter diffraction (EBSD) was carried out to investigate the texture utilizing a HKL Nordlys orientation imaging microscope system (Oxford Instruments, UK) mounted on SEM. The scanning step was determined at 0.5 μm. Before EBSD measurement, the samples suffered mechanical polishing, and subsequent electrolytic
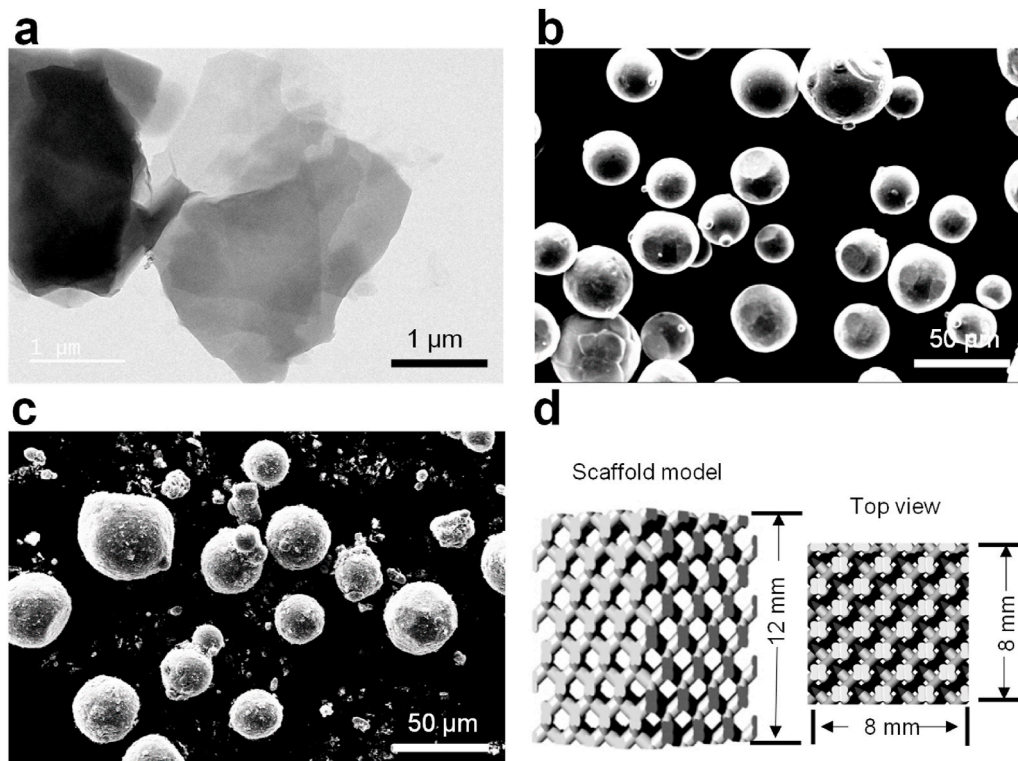

Fig. 1. (a) TEM image showing the as-received RGO; (b–c) SEM images showing the Zn and Zn-RGO mixed powders; (d) The scaffold model utilized for LPBF.

polishing at room temperature. A mixture of 50% orthophosphoric acid and 50% alcohol was used as electrolyte, and platinum plate was used as cathode. Besides, transmission electron microscope (TEM, TecnaiG2-20, FEI Company, USA) was used to further study the microstructure at 200 kV. In detail, the samples were cut into 1 mm thick slices by wire cutting, and further polished to 50–60 μm with sandpaper, and then punched to make a disc with a diameter of 3 mm. The sample was putted into ion milling device (Gatan 695) for thinning with an initial angle of $\pm 4°$ and voltage of 5 kV. As the small holes appeared, it was adjusted to $\pm 1°$ and 3 kV, and kept for 10 min.

2.4. Mechanical tests

According to the ISO 13,314:2011 standard, scaffolds were adopted for compressive tests using an electronic universal testing machine (2 mm/min, 10 kN). The elastic modulus was defined as slope of the initial elastic straight line, whereas the ultimate strength was determined at the first maximum compressive strength. Zn slabs were shaped into tensile samples according to the ASTM 8E standard. The tensile tests were performed at a head speed of 1.5 mm/min. The facture surface obtained from tensile tests was captured by SEM. Indentation measurements were carried out utilizing a microhardness tester with a loading of 1 N.

2.5. Electrochemical and immersion experiments

Electrochemical experiments were performed on electrochemical equipment (CHI604D, CH Instruments Ins., China) aiming to estimate the corrosion behavior. The sample, platinum sheet and Ag/AgCl/in saturated KCl electrode served as the working electrode, counter electrode and reference electrode, respectively. Simulated body fluids (SBF) were used as electrolytic solution at 37 °C. The samples were tested to obtain the open circuit potential (OCP) with an exposure area of 10×10 mm^2. Afterwards, the Tafel curves were recorded within the range of OCP± 300 mV. The corroded surface was observed using SEM after removing the corrosion products. Besides, the electrochemical impedance spectroscopy tests were performed over a frequency range of 10^{-2} to 10^6 Hz with a perturbation of 1 mV.

Immersion tests were performed to further study the degradation behavior according to ASTM G31-72. After soaking for 3, 7 and 14 days, the Zn ion concentration during immersion was determined using inductively coupled plasma-atomic emission spectroscopy (ICP-AES, Thermo Elemental).

2.6. In vitro cell tests

Umbilical cord mesenchymal stem cells were used to evaluate the cell response of Zn and Zn-RGO scaffolds. DMEM supplemented with 10% fetal bovine serum, 100 U/mL of penicillin and 100 mg/mL of streptomycin were used as culture medium. The cells were directly cultivated on the scaffolds and incubated in humid environment at 37 °C, with culture medium renewed every other day. After culture for 1, 4, and 7 d, the cells were digested for 1 min with 0.25% Trypsin to detach from the scaffolds, and washed using the phosphate buffer saline (PBS). The collected cells were stained using Calcein-AM and Ethidium homodimer-1 reagents for 20 min, and then mounted on the glass slides and observed using a microscopy (BX60, Olympus Co., Japan). The cell counting kit-8 (CCK-8) assay was performed to study the cell proliferation. At 1, 4, and 7 d, the cells were washed from the scaffolds, and further cultured for another 2 h with 10 μL of CCK-8. The absorbance at 450 nm was then determined using a paradigm detection platform (Beckman Coulter Inc., USA). In addition, the alkaline phosphatase (ALP) staining was also carried out to investigate the cell differentiation. At 4, 7 and 14 d, the total protein content and the ALP of cells on scaffolds were determined using the microplate reader.

2.7. Statistical analysis

All the experiments, including mechanical tests, electrochemical experiments and cell experiments, were performed at least three times to obtain the averages. The statistical significance was investigated using student's t-test method, in which p less than 0.05 was recognized to be statistically significant.

3. Results and discussion

3.1. The quality of RGO

XPS analysis showed that GO contained ~33.90 at.% of oxygen, which was due to its numerous oxygen-containing functional groups including carboxylate carbon (O=C–O), the carbonyl carbon (C=O) and *C*–O bonds. During the thermal treatment, the color of suspension changed from brown to dark gray, as showed in Fig. 2a. It was believed that a part of oxygen-containing functional groups attached on carbon plane decomposed at elevated temperature [27]. As XPS analysis proved, the as-received RGO powder had a reduced oxygen content of 8.70 at.%. The XRD spectrum was presented in Fig. 2c. A strong diffraction peak (11.7°) appeared in GO with a large interlayer spacing, owing to the presence of oxygen functional groups [28]. As a comparison, a broad peak located at 25.8° was observed in RGO, indicating its reduced interlayer spacing. The corresponding Raman spectra were showed in Fig. 2d. The peaks located at 1345 cm^{-1} and 1590 cm^{-1} corresponded to D band and G band, respectively. It should be noted that the intensity ratio of D/G was increased from 0.993 to 1.107, which revealed that the average size of sp2 carbon domain was decreased for RGO [29]. As compared with GO, RGO possessed a large surface area and strong mechanical strength and elastic modulus [30,31]. On the other hand, as compared with graphene, RGO still contained oxygen-containing functional groups, which was expected to promote the cell behavior [32]. Thus, RGO was used as reinforcement in this work.

3.2. Microstructure and texture of Zn-based scaffolds

The typical Zn-based composite scaffold fabricated by LPBF was presented in Fig. 3a, which exhibited a three-dimensional pore structure with a strut size slightly larger than 500 μm (Fig. 3b). The as-built scaffold was treated by sandblasting, which could remove the unmelted powder particles attached on the struts and improve the scaffold surface quality, as proved by the SEM images. Usually, a large amount of partially melted particles would adhere on the struts, since the surrounding particles preferred to approach the liquid pool during LPBF [33]. The strut was polished using metallographic sandpaper, and then observed by SEM to investigate the relative density, as showed in Fig. 3c. No obvious defect such as cracks or pores was observed within the strut, which indicated the high densification. As reported by previous research, the densification rate of Zn part fabricated by laser additive manufacturing could achieve ~99.5% at optimal processing parameter [34]. To investigate the distribution of RGO in matrix, the polished Zn matrix was captured by SEM at high magnification, as showed in Fig. 3d. For the Zn-0.1RGO and Zn-0.2RGO, some small and lamellar particles were uniformly distributed in the matrix. The EDS analysis (line A-A) revealed these particles were rich in C, which proved that they should be incorporated RGO. However, RGO at an increased content of 0.3 wt% tended to agglomerate in the matrix, which was ascribed to the strong π–π interactions and huge van der Waals force [35,36].

EBSD analysis was performed to investigate the texture, and the obtained inversed pole figures were presented in Fig. 4a, which revealed the grain orientation along the building direction. Herein, the red, green and blue color levels were proportional to the three basic orientations of (0001), (10$\bar{1}$0) and (12$\bar{3}$0), respectively. Clearly, the obtained map of Zn
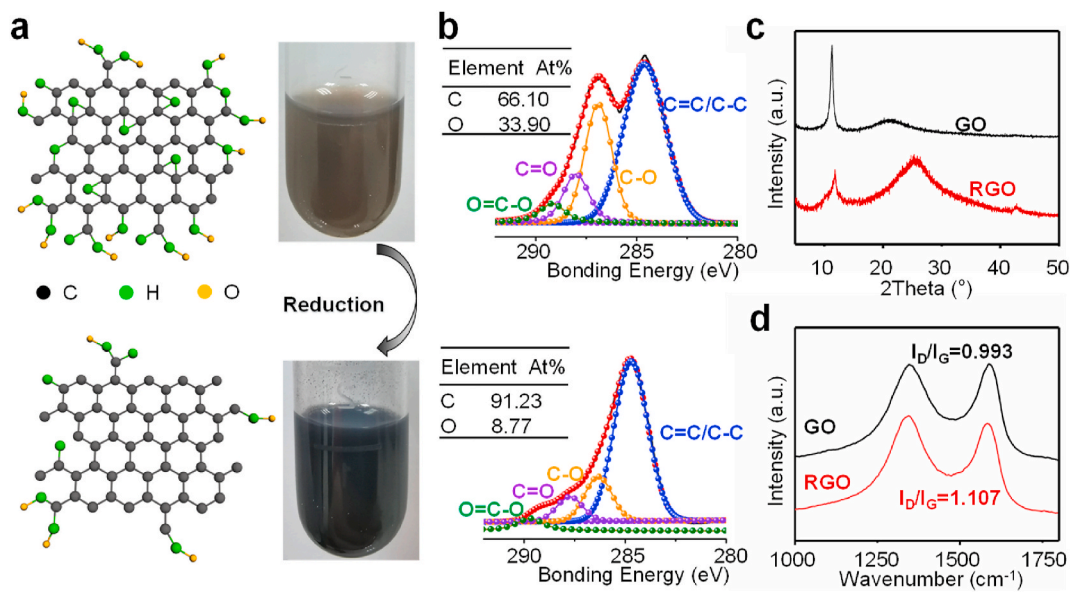
Fig. 2. (a) Schematic of GO and RGO. The inserts showed their suspension, which turn from brown to dark gray after thermal treatment; (b) XPS analysis indicated that the oxygen content significantly was reduced after thermal treatment; (c) XRD and (d) Raman spectrum of GO and RGO.

part was dominated by red color, which indicated it inclined to grow into (0001) orientation. The grain orientation highly depended on the maximum heat transfer direction during rapid solidification, and was usually perpendicular to the melt pool boundary [34]. Thus, the grains tended to grow along the building direction for the laser processed Zn. However, in Zn-RGO composite, the grain orientation along (0001) turned weak. Particularly, the Zn-0.2RGO exhibited more random orientation with a combination of the three basic grain orientations. These results indicated that the addition of RGO affected the texture of Zn part fabricated by LPBF.

In order to understand the liberalization degree of orientation, the pole figures along building direction were showed in Fig. 4b. The texture index (TI), namely the fibrous texture intensity, was calculated by Refs. [37]:

$$\mathrm{TI} = \int_{eulerspace} (f(g))^2 dg \tag{1}$$

where $f(g)$ was the orientation distribution as a function of the Euler space coordinates (g). The LPBF-processed Zn displayed a strong fiber texture with a TI of 20.5. Such a strong fiber texture was believed to be detrimental to the ductility, since there were few grains placed in orientations that benefited for basal slip. In control, Zn-0.2RGO showed decreased texture intensity with TI reducing to 7.3. In general, a weak texture, namely random grain orientation, would result in the improvement of isotropy in metal matrix [38]. The improved texture randomization was due to the heterogeneous nucleation effect of RGO. The nucleation of new grains at the solidification frontier generally required numerous nucleation sites and an energetically favorable condition. Usually, the undercooling at solidification front was able to provide an energetically favorable condition [39]. After incorporating RGO, the undercooling at the interface was significantly enhanced owing to the high thermal conductivity of RGO. As a consequence, RGO nano sheets acted as low-energy-barrier heterogeneous nucleation sites ahead of the solidification front and induced the fine equiaxed grain growth [40]. The formation of new grains with varied orientation against the original one could accommodate more strain under tensile loading. Thus, it was expected to tailor the texture thus improving the ductility.

The map of grain boundary misorientation angles were presented in Fig. 5. It could be seen that LPBF-processed Zn was mainly composed of columnar grain, which was also reported by other literature [34]. After adding a small amount of RGO, finer equiaxed grains were observed in the matrix. It was because that RGO pinned at the grain boundaries and disturbed the grain growth along one single direction. However, a large amount of fine columnar grains formed with RGO further increasing to 0.3 wt%. A fact was that the thermal conductivity of RGO (~373–1056 W/(m·K)) was one order of magnitude higher than that of Zn (~116 W/(m·K)) [41]. Thus, the agglomerated RGO at the frontier of the solid/liquid interface would guide the crystal to penetrate into the liquid in the local area, thereby inducing the formation of columnar grain [37].

The average grain size was quantitatively analyzed by using the Channel 5 software. LPBF-processed Zn exhibited an average grain size of ~6.9 μm. As compared with Zn fabricated by conventional process, such as casting and powder metallurgy, LPBF-processed Zn possessed fine grain, which was owing to the rapid solidification rate. Significantly, the average grain sizes decreased to 3.1 μm for Zn-0.2RGO and 2.4 μm for Zn-0.3RGO. The boundaries were color-coded with low-angle grain boundaries (LAGBs) in green and high-angle grain boundaries (HAGBs) in black (Fig. 5). In this study, grain boundaries misorientation angle above 10° was defined as HAGBs, whereas the misorientation angle between 2° and 10° was defined as LAGBs. It was revealed that the fraction of HAGBs gradually increased from 53.31% for Zn to 72.18% for Zn-0.2RGO. However, a sharp decrease to 51.85% occurred for Zn-0.3RGO. It was believed that the excessive RGO led to the nucleation of numerous sub crystals, thus forming a large number of LAGBs. Nevertheless, HAGBs could effectively limit crack propagation, which might exert a positive effect on the mechanical properties.

3.3. Mechanical property

The compressive properties of LPBF processed Zn and Zn-RGO scaffolds were assessed. As subjected to compressive stress, all the samples presented continuous and smooth stress-strain curves, as depicted in Fig. 6a. In detail, all the curves started with a sharp slope, which was recognized as the elastic region, and then experienced a plateau stage without obvious fluctuations. The corresponding yield strength and elastic modulus derived from the compressive curves were showed in Fig. 6b. Zn scaffold presented a relatively low yield strength and elastic modulus of 11.7 ± 0.4 MPa and 762.5 ± 20.1 MPa, respectively, which was related with its high porosity (~69.7% as calculated by the scaffold model). It was reported that LPBF processed Zn scaffold
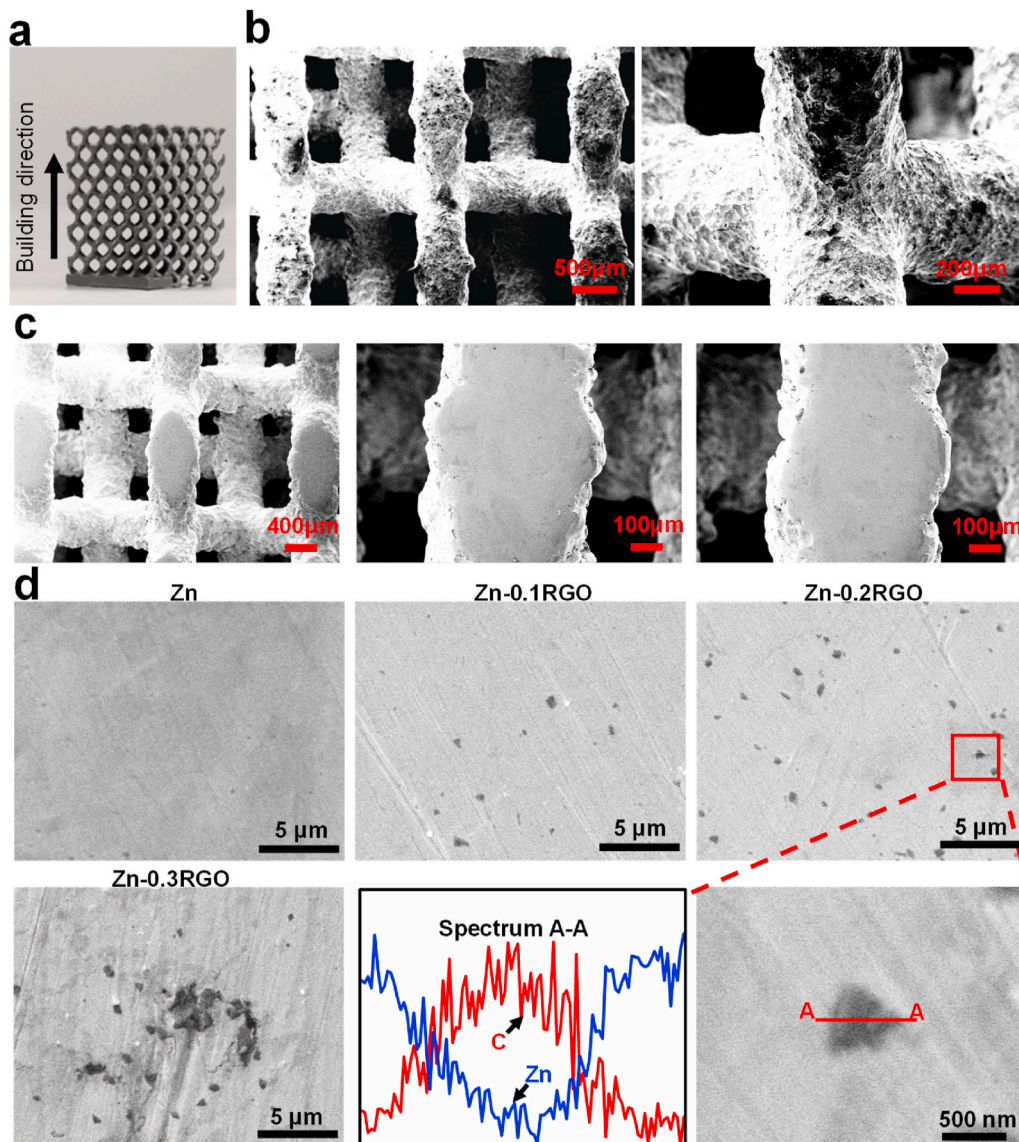
Fig. 3. (a) As-built scaffold; (b) SEM images (Top view) showing the surface of LPBF-processed scaffold; (c) Low-magnification SEM images showing the strut after polishing; (d) High-magnification SEM images showing the distribution state of RGO in Zn matrix. The EDS analysis was performed on the line A-A, as marked in Fig. 3d.

with a porosity of 70% showed a comparable yield stress of 11.8 MPa and an elastic modulus of 785.7 MPa [42]. It should be noted that the yield strength and elastic modulus were gradually enhanced to 19.1 ± 0.7 MPa and 1124.9 ± 30.2 MPa, respectively, for Zn-0.2RGO scaffold. The tensile tests were also performed using the spline samples without pore structure, with typical tensile stress-strain curves depicted in Fig. 6c, and the corresponding tensile properties were listed in Table 1. It could be seen that the tensile yield strength and fracture elongation were simultaneously enhanced after incorporating RGO. A comparison of Zn parts fabricated by various processing methods was also listed in Table 1. Laser additive manufactured Zn showed high mechanical properties as compared with those prepared by other processing methods, such as casting, rolling and extrusion. As mentioned above, LPBF obtained fine grains owing to its extremely high cooling rate, thus contributing to the improvement of mechanical properties through fine grain strengthening. Besides, the hardness was tested, with results showed in Fig. 6d. Clearly, the hardness gradually increased after incorporating RGO.

The above results showed RGO significantly enhanced the

mechanical strength of the LPBF-processed Zn-based composites. The mechanical strength of a material was closely related with the presence and scale of the obstruction that resisted the dislocation motion in matrix. Herein, the grain refinement strengthening should undoubtedly account for the enhanced strength of Zn-RGO. Grain refinement strengthening was also recognized as grain boundary strengthening, which was essentially caused by the hindrance of grain boundaries to dislocations. The relationship between grain size and yield strength could be determined by Hall-Petch law, which had been thoroughly described in other literatures [46,47]. As presented in Fig. 5, LPBF processed Zn-0.2RGO exhibited considerably refined grains as compared with Zn. Consequently, the external stress to activate the dislocations of grain boundaries would significantly increase, thus exhibiting enhanced yield strength. Furthermore, a remarkably high fraction of HAGBs was observed in Zn-0.2RGO. Comparing with LAGBs, HAGBs could availably inhibit the dislocation slip and induce the dislocation entanglement near the boundaries, which should also be favorable for the strength enhancement of Zn-RGO [48].

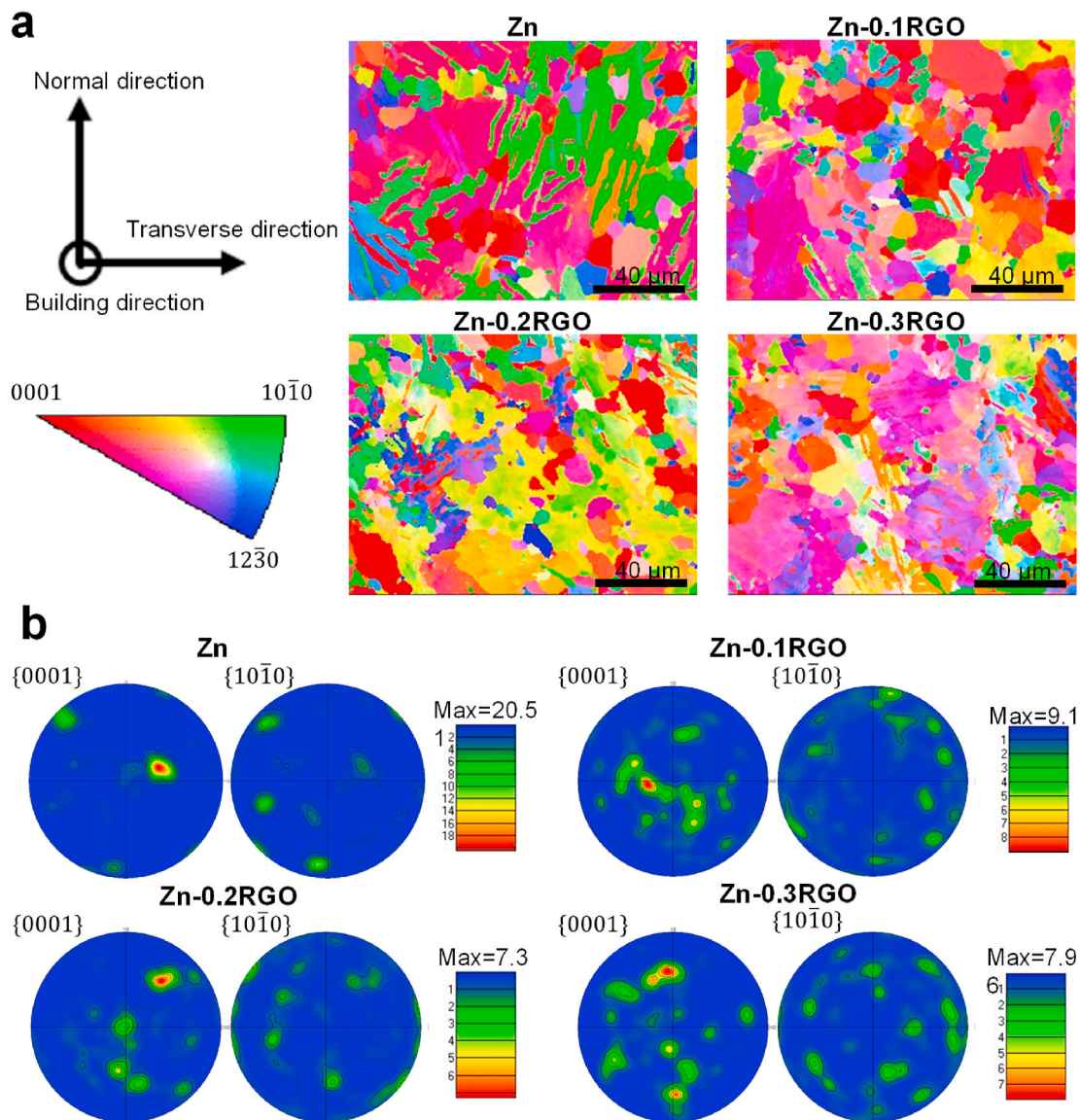The load transfer effect caused by the incorporated RGO was also

Fig. 4. (a) Inversed pole figures and (b) pole figures of Zn and Zn-RGO. All the maps were observed along the building direction.

responsible for the enhancement of mechanical strength. It was well known that the exerted stress would shift from the matrix to the reinforcement by means of interfacial shear stress [49]. An efficient load shift was strictly dependent on (i) the aspect ratio of the reinforcement, and (ii) the interfacial bonding between the matrix and reinforcement. In this work, RGO with two-dimensional feature possessed an extremely huge aspect ratio, as compared with commonly-used reinforcements such as nanoparticles and nanorods. Particularly, RGO with wrinkled surface could effectively cause mechanical interlock with matrix [50]. TEM was used to observe the interface between RGO and Zn matrix. The favorable interface bonding without obvious gaps or voids formed between RGO and Zn matrix, as presented in Fig. 7a and b. It was also revealed that RGO maintained the original hexagonal structure, namely honeycomb lattice, as highlighted in Fig. 7b. These results confirmed that the LPBF process had no structural damage to RGO. Considering previous researches, oxygen-mediated bonding, as illustrated in Fig. 7c, was the main bonding mechanism between RGO and metal matrix [51]. The oxygen in oxygen-mediated bonding was derived from the oxygen-containing functional groups of RGO. A theory calculation proved that the oxygen functional group was able to enhance the interface binding by means of promoting the electron exchange between

carbon atoms and metal matrix [52].

With the aid of efficient load transfer, several possible strengthening mechanisms of RGO were proposed, as schematically depicted in Fig. 7d. In general, the essence of the reinforcement by RGO was to prevent the crack propagation. As cracks propagated to the vicinity of RGO, the load would be transferred from the matrix to RGO because of the much higher elastic modulus of RGO than that of Zn. RGO would be fractured once the external force exceeded the critical strain. Furthermore, the crack deflection might occur along the interface when the RGO pulled out the matrix. As the cracks continually propagated, its energy was not enough to separate the RGO from the matrix. In this case, the RGO would act as an "elastic bridge" and limit the further spread of cracks [53]. Owing to the huge specific surface area and good interface bonding, the strengthening mechanism discussed above would consume massive fracture energy, which significantly limited the crack propagation in Zn-RGO matrix. Thereby, Zn-RGO exhibited a considerably enhanced load-bearing ability.

Besides, the Orowan strengthening caused by homogeneously distributed RGO should also be taken into consideration. The essence of Orowan strengthening was to use the dispersed ultrafine particles to block the movement of dislocations [54]. However, in present work, the
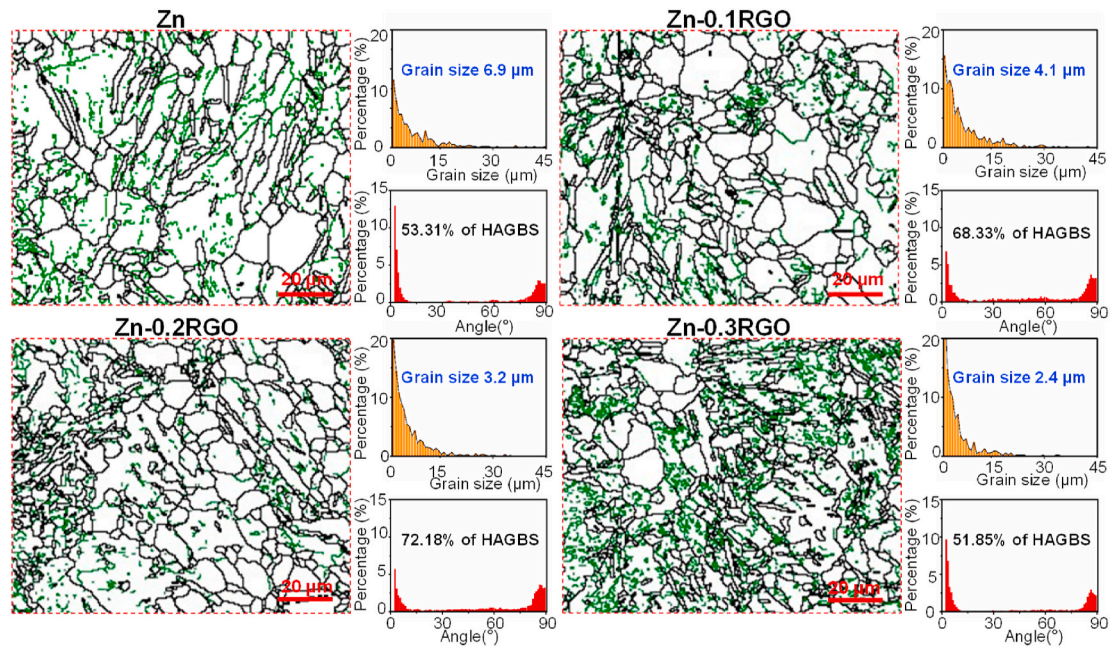
Fig. 5. Grain boundary maps of the Zn and Zn-RGO obtained from BESD analysis. The black represented the HAGBs, whereas the green represented the LAGBs. The grain size and grain boundary misorientation angles were also analyzed.
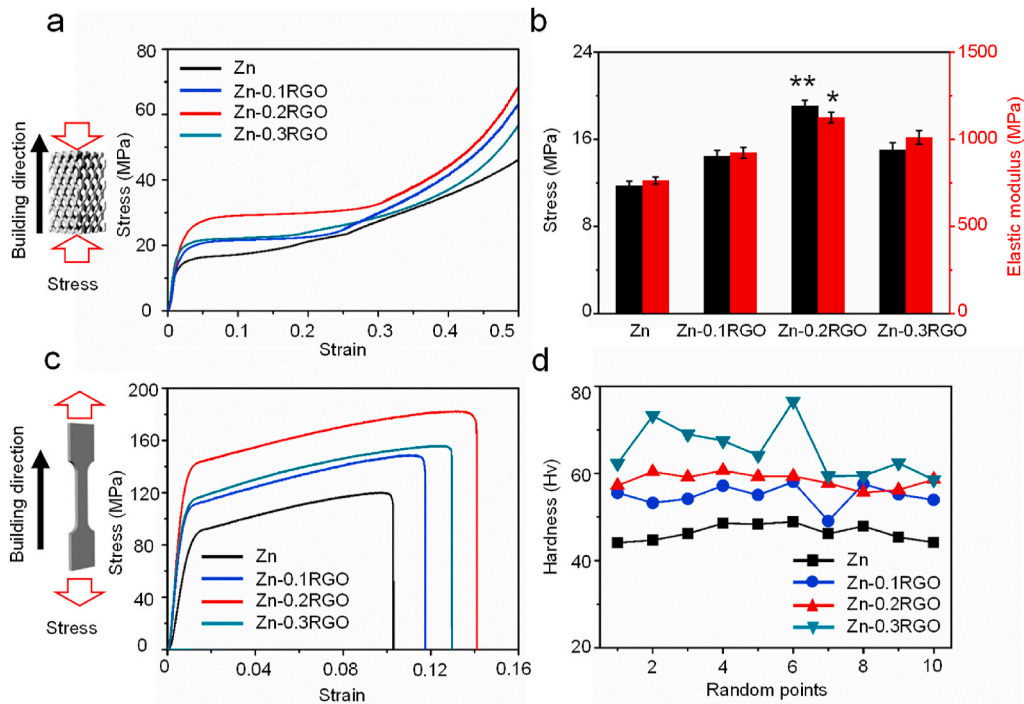

Fig. 6. (a) Representative compressive curves of the Zn and Zn-RGO scaffolds; (b) The corresponding compression strength and elastic modulus; (c) Typical tensile curves of the Zn, and Zn-RGO samples; (d) Vickers hardness. N = 3, p*<0.05, p**<0.01 (Zn as control).

incorporated RGO showed large inter-particle space owing to their two dimensional structure and coarse diameters ranging from 0.3 to 2 μm. From this aspect, the improvement of mechanical strength caused by Orowan strengthening was relatively low as compared with the other two factors discussed above. In a word, the incorporated RGO generated numerous dislocations and consequently produced a quantity of obstacles to limit the movement of dislocation, and beard more stress-loading of the matrix, thus significantly improving the mechanical strength of the composites. Nevertheless, such an enhancement effect was impaired

in Zn-0.3RGO. Usually, there was a critical value of nano reinforcement in composites for the strengthening effect [55,56]. As the quantity of nano reinforcement below the critical value, they homogeneously distributed in the matrix, and effectively enhanced the matrix strength. Once beyond the critical value, the nano reinforcement agglomerated in the matrix, due to the high surface area and van der Waals force. In present work, the critical value of RGO in Zn matrix was believed to be 0.2 wt%. Thus, Zn-0.2RGO exhibited the best mechanical properties. Interface compatibility between nano reinforcement and matrix was the

Table 1
The tensile properties of Zn-based parts obtained by various processing methods.

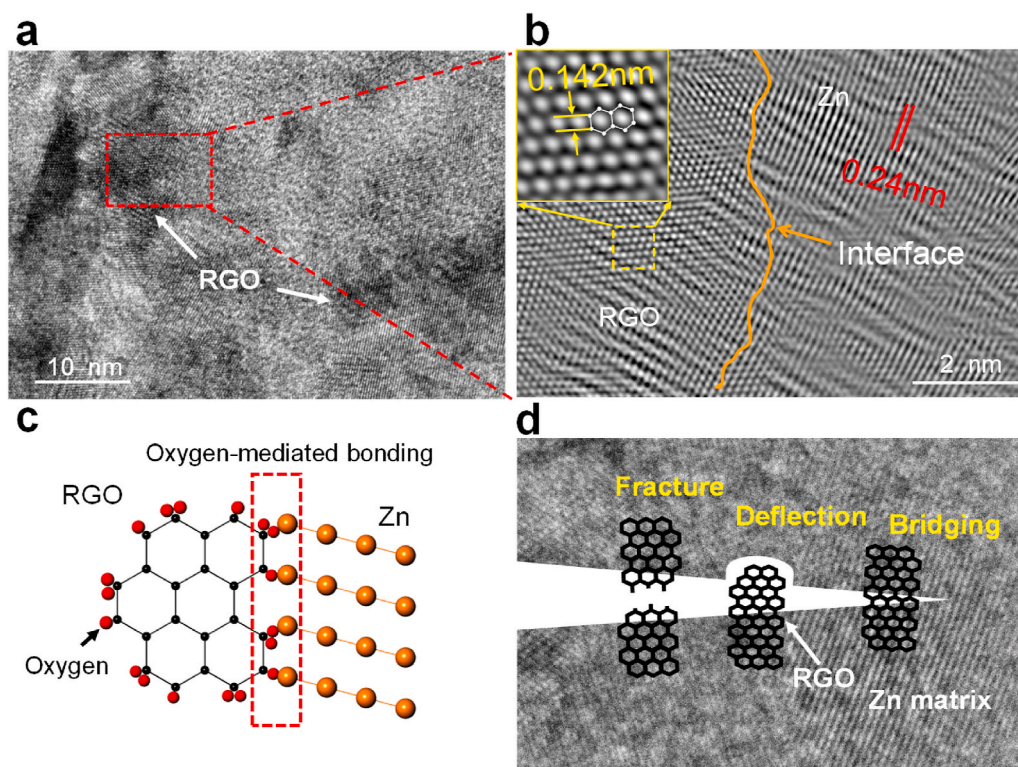| Sample	Yield strength (MPa)	Ultimate tensile strength (MPa)	Elongation (%)	Processing method
Zn	91.6 ± 7.3	119.9 ± 8.5	9.5 ± 1.0	LPBF
Zn-0.1RGO	111.3 ± 9.1	148.5 ± 10.6	11.7 ± 1.2	LPBF
Zn-0.2RGO	142.9 ± 13.4	182.1 ± 15.4	14.1 ± 1.8	LPBF
Zn-0.3RGO	115.7 ± 17.5	155.2 ± 18.1	12.9 ± 2.3	LPBF
Zn [43]	10 ± 2	18 ± 3	0.3 ± 0.1	Casting
Zn [43]	30 ± 7	50 ± 9	5.8 ± 0.8	Rolling
Zn [44]	51 ± 4	111 ± 5	60 ± 6	Extrusion
Zn [34,45]	114 ± 4	134	10.1	LPBF

Fig. 7. (a–b)TEM images showing the interface bonding of RGO in Zn matrix; (c) The schematic showing the oxygen-mediated bonding between Zn and RGO; (d) The possible strengthening mechanisms of RGO, which could effectively limit the crack propagation in the composite.

key point to achieve their homogeneous dispersion. In fact, substantial improvement in interface adhesion between RGO and metal matrix through the introduction of interfacial carbides has been reported [57, 58].

The strengthening of composites usually led to a decreased ductility. Encouragingly, in this work, the Zn-RGO exhibited a simultaneously increased strength and ductility as compared with pure Zn. It was well accepted that the basal slip was the prime plastic deformation strategy for Zn with close packed hexagonal structure [59]. However, as presented in Fig. 4, LPBF processed Zn possessed strong fiber texture, which exerted a negative influence on the basal slip activation [60]. In control, Zn-RGO composite exhibited a weakened fiber texture, which should induce twins and vigorously activate the basal slip. Meanwhile, Zn-RGO with increased grain boundaries provided enough space for basal slip dislocation. On the other hand, the activation of non-basal slip systems could also enhance the ductility of Zn. As showed in Fig. 8, numerous cleavage steps presented on the tensile fracture of Zn, indicating its brittle characteristic. In control, a large amount of dimples appeared on the fracture of Zn-0.2RGO. It was clearly evident that Zn-0.2RGO with a weakened fiber exhibited a ductile plastic deformation, since a significant amount of non-basal slip was triggered by RGO. In brief, the incorporation of RGO enhanced the ductility by tailoring the

microstructure and texture. Alloy treatment could also achieve the improvement of strength and ductility by the means of solid solution strengthening. Nevertheless, for common solution alloying element, such as Al, it might cause cell toxicity problem [61]. As for alloying element with favorable compatibility, such as Mg and Fe, the solid solution in Zn matrix was very limit [62,63]. Unlike alloying element, RGO served as powerful nano reinforcement, and was also expected to bring a positive role for cell growth.

3.4. Degradation behavior

The bone scaffolds deserve a favorable biodegradability, aiming to be completely absorbed after implantation in vivo thus serving as a temporary substitute. Zn degrades by means of corrosion in physiological environment. Thereby, electrochemical test was carried out to estimate the degradation behavior of Zn-0.2RGO, with pure Zn as control. The obtained electrochemical polarization curves were depicted in Fig. 9a, and the derived corrosion parameters, including corrosion potential (E_{corr}) and corrosion current density (i_{corr}), were listed in Table 2. As compared with Zn, Zn-0.2RGO exhibited enhanced i_{corr} and decreased E_{corr}, which indicated that the incorporated RGO enhanced the driving force of electrochemical corrosion in Zn matrix. The
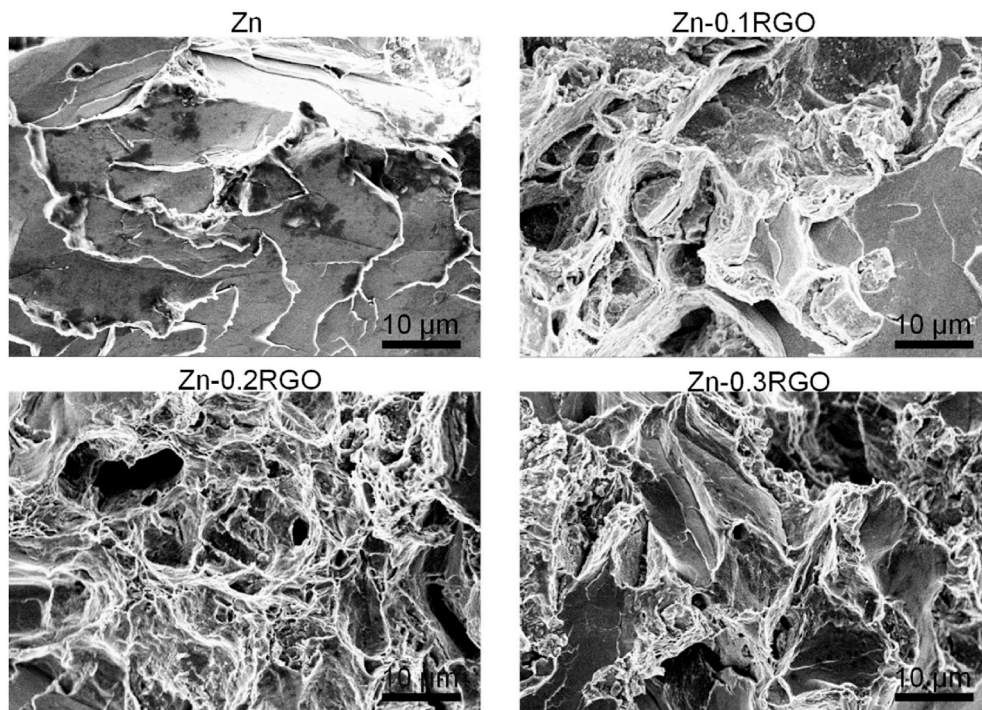
Fig. 8. SEM images showing the fracture surface of Zn and Zn-RGO samples after tensile tests.
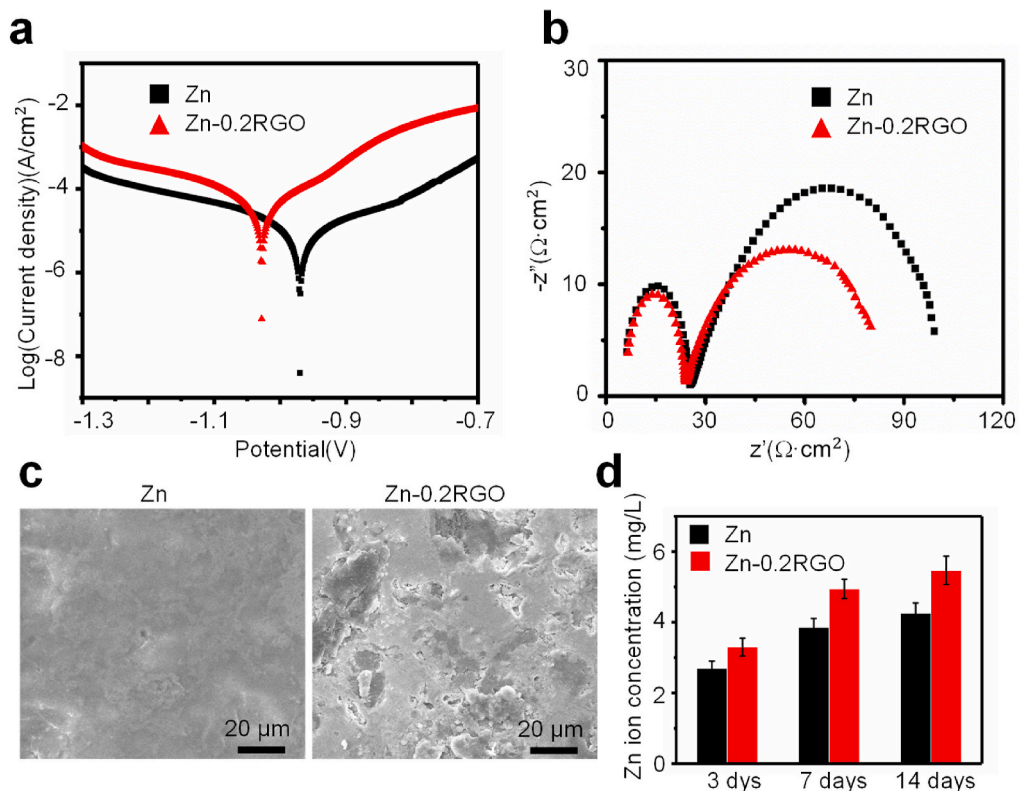

Fig. 9. (a) Polarization curves, (b) Nyquist plots and (c) corroded surface of Zn and Zn-RGO obtained from electrochemical experiments; (d) The Zn ion concentration during soaking in SBF.

obtained Nyquist plots were depicted in Fig. 9b, which showed two continuous semicircles. The Nyquist plot for Zn-RGO exhibited relatively small semicircle diameter, which It also represented the reduced corrosion resistance. The corroded surface after the polarization was captured by SEM, as exhibited in Fig. 9c. Few corrosion holes appeared on Zn part, indicating its relatively slight and uniform corrosion. As a comparison, numerous small corrosion pits presented on Zn-0.2RGO part, which proved the occurrence of severe local corrosion during polarization.

A comparison between the electrochemical corrosion parameters of

Table 2

A comparison between the electrochemical corrosion parameters of LPBF processed Zn, Zn-RGO and other biodegradable metal.

Sample	E_{corr} (V)	i_{corr} (μA/cm²)	Corrosion rate (mm/year)	Electrolyte solution	References
Zn	-0.96 ± 0.06	7.48 ± 1.37	0.11 ± 0.02	SBF	In this work
Zn-0.2RGO	-1.03 ± 0.08	18.6 ± 2.32	0.27 ± 0.03	SBF	In this work
Casted Zn	-0.99	9.20	0.14	Hanks	[44]
Rolled Zn	-1.35	10.96	0.16	SBF	[64]
Fe alloy	-0.387	0.652	0.008	Hanks	[65]
Mg alloy	-1.59 ± 0.04	31.24 ± 4.21	0.71	SBF	[66]

LPBF processed Zn, Zn-RGO and other biodegradable metal was also listed in Table 2. LPBF-processed Zn showed a slightly increased degradation rate, as compared with that fabricated by other process. It was speculated that the grain refinement enhanced the corrosion tendency of Zn. High-density grain boundaries possessed more amorphous regions, which usually suffered intergranular corrosion. However, the relationship between the grain size and the degradation rate of Zn had not been verified. On the other hand, as compared with Mg and Fe alloy, Zn exhibited an intermediate E_{corr} and consequently a more mild degradation rate. Our results also revealed that the RGO enhanced the corrosion rate of Zn matrix. The accelerated electrochemical corrosion was mainly attributed to two aspects: (i) The grain refinement effect caused by the addition of RGO was conducive to accelerate the electrochemical corrosion; (ii) RGO and Zn matrix formed numerous microgalvanic cells in local area thus further improving the corrosion.

Immersion tests were performed and the variations of Zn ion concentration were depicted in Fig. 9d. After soaking for 14 days, the Zn ion concentration was gradually increased to 5.47 mg/L for Zn-0.2RGO group, which was slightly higher than that of Zn group. It was reported that the Zn ion concentration below 12.1 mg/L showed no obvious cytotoxicity [67]. As implanted in vivo, Zn would be gradually degraded, and RGO would be detached from the Zn matrix, and then dispersed in the body fluid. The dispersed carbon materials was able to achieve complete metabolism in blood by human myeloperoxidase, eosinophil peroxidase, lactoperoxidase and xanthine oxidase, since the nanosheets were pushed to the catalytic site following interaction of its carboxyl groups with amino acids in enzyme [68]. On the other hand, graphene nano sheets with abundant functional groups were easy to adhere to the cell membrane and then be uptake by cells [69].

3.5. In vitro biocompatibility

Bone implants require good biocompatibility so as to provide a good environment for cell proliferation and growth [70–72]. Herein, the cell behavior of Zn-0.2RGO scaffold was evaluated, with Zn scaffold as control. The cells after culture for 1, 4, 7 days were digested from the scaffold and visualized by fluorescence microscope, as presented in Fig. 10a. The live cells were stained in green, whereas the dead cells were stained in red. There were very a few of dead cells at day 1 and day 4. Clearly, the cells increased significantly with the prolongation of culture period. At 4 and 7 days, the cells formed a large amount of filopodia. CCK-8 assay was used to quantitatively analyze the cell growth, with results showed in Fig. 10b. With culture time extending, the detected optical density gradually increased, indicating the normal cell proliferation. Particularly, the optical density obtained from Zn-0.2RGO scaffold group was considerably higher than that on Zn scaffold group at day 7 (*p < 0.05). All these results proved that Zn-0.2RGO scaffold provided a more favorable environment for cell growth. The cell differentiation behavior was investigated by determining the ALP activity (Fig. 10c). Clearly, the cells cultured on Zn-RGO scaffold exhibited a significantly improved ALP activity than that on Zn scaffolds at day 7 and day 14, which revealed that the Zn-RGO scaffold
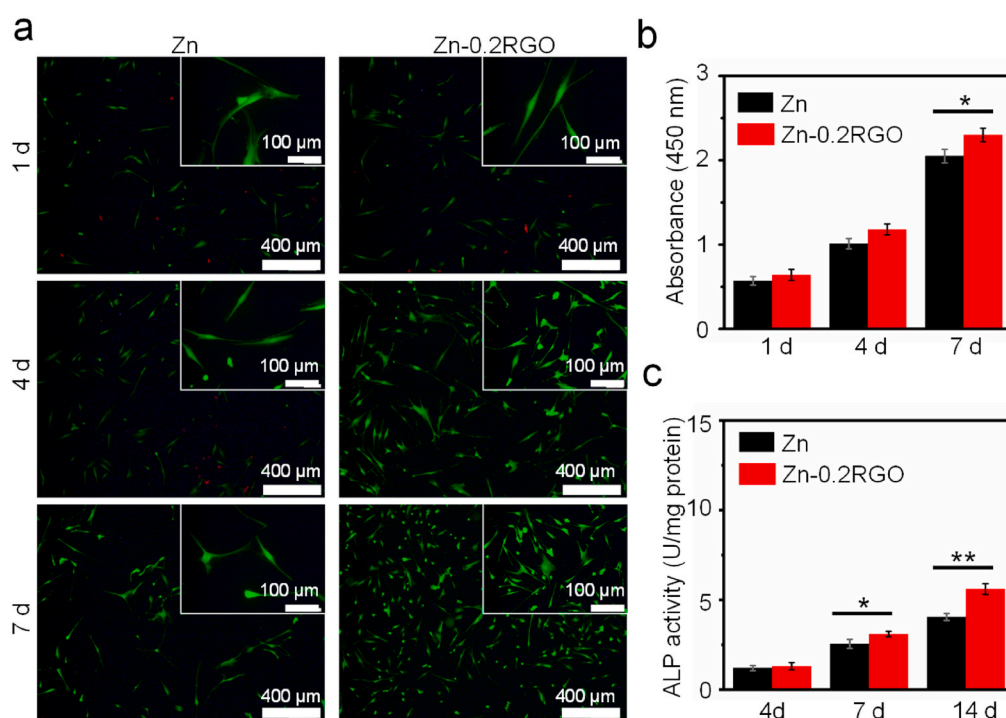

Fig. 10. (a) Fluorescence images of cells obtained from LIVE/DEAD tests, in which the live cells were stained in green and dead cells in red; (b) CCK-8 results and (c) ALP activity. N = 3, *p < 0.05, **p < 0.01.

promoted cell differentiation.

The above results proved that Zn-RGO scaffold was more beneficial for cell adhesion, growth and differentiation, despite its accelerated degradation and excessive ion release. It was believed that the incorporated RGO exerted a positive effect on cell behavior. An undeniable fact was that RGO still contained a large amount of oxygen-containing functional groups. These negatively charged oxygen-containing functional groups was able to interact with cell membrane phospholipids and proteins by means of electrostatic interaction, hydrogen bonding, p-p stacking, etc [73]. Hence, the RGO-contained scaffold with enhanced bioactivity was favorable for cells adhesion and growth as compared with Zn scaffold, which overshadowed the negative effect of accelerated degradation. Previous researches also proved that RGO could lead to the change of gene expression regulated by non-coding RNA in the cytoplasm, thus promoting the differentiation of stem cells [74,75]. In brief, the incorporated RGO exerted a beneficial effect on the biological properties of Zn-based scaffold for bone tissue engineering.

4. Conclusion

In this study, Zn-RGO scaffold was successfully fabricated via laser additive manufacturing process. Our results clearly proved that RGO played an important role in tailoring the microstructure and enhancing the mechanical performance. The conclusions could be drawn as follows:

(1) The homogeneously distributed RGO contributed to the grain refinement and the weakened texture, since the RGO pinned at the grain boundaries and induced equiaxed growth of grains.

(2) The RGO-induced grain refinement, and the efficient load transfer caused by the huge specific surface area of RGO and the favorable interface bonding were the two primary strengthening factors that improved the mechanical strength of Zn. At the same time, RGO activated more slip systems in Zn matrix and simultaneously improved the ductility of composites.

(3) The incorporated RGO improved the cell behavior of Zn scaffold, including cell growth and differentiation, owing to the positive effect of the oxygen-containing functional groups. It also enhanced the corrosion rate due to the grain refinement as well as micro-galvanic effect.

CRediT authorship contribution statement

Youwen Yang: Conceptualization, Investigation. **Yun Cheng:** Investigation. **Shuping Peng:** Investigation, Data curation. **Liang Xu:** Formal analysis. **Chongxian He:** Investigation, experiments. **Fangwei Qi:** Investigation. **Mingchun Zhao:** Resources. **Cijun Shuai:** reviewing and .

Declaration of competing interest

The authors declare that they have no known competing financial interests or personal relationships that could have appeared to influence the work reported in this paper.

Acknowledgement

References

[1] Y. Zheng, X. Gu, F. Witte, Biodegradable metals, Mater. Sci. Eng. R Rep. 77 (2014) 1–34.

[2] Y. Zhang, L. Tan, Q. Wang, M. Gao, I.P. Etim, K. Yang, Effects of microstructure on the torsional properties of biodegradable WE43 Mg alloy, J. Mater. Sci. Technol. 51 (2020) 102–110.

[3] A. Atrens, S. Johnston, Z. Shi, M.S. Dargusch, Understanding Mg corrosion in the body for biodegradable medical implants, Scripta Mater. 154 (2018) 92–100.

[4] C. Shuai, B. Wang, S. Bin, S. Peng, C. Gao, TiO2-Induced in situ reaction in graphene oxide-reinforced AZ61 biocomposites to enhance the interfacial bonding, ACS Appl. Mater. Interfaces 12 (20) (2020) 23464–23473.

[5] J. Venezuela, M. Dargusch, Addressing the slow corrosion rate of biodegradable Fe-Mn: current approaches and future trends, Curr. Opin. Solid State Mater. Sci. (2020) 100822.

[6] C. Shuai, S. Li, W. Yang, Y. Yang, Y. Deng, C. Gao, MnO2 Catalysis of Oxygen Reduction to Accelerate the Degradation of Fe-C Composites for Biomedical Applications, Corrosion Science, 2020, p. 108679.

[7] D. Zhu, Y. Su, M.L. Young, J. Ma, Y. Zheng, L. Tang, Biological responses and mechanisms of human bone marrow mesenchymal stem cells to Zn and Mg biomaterials, ACS Appl. Mater. Interfaces 9 (33) (2017) 27453–27461.

[8] L. Zhao, X. Wang, T. Wang, Y. Xia, C. Cui, Mechanical properties and biodegradation of porous Zn-1Al alloy scaffolds, Mater. Lett. 247 (2019) 75–78.

[9] H. Yang, B. Jia, Z. Zhang, X. Qu, G. Li, W. Lin, D. Zhu, K. Dai, Y. Zheng, Alloying design of biodegradable zinc as promising bone implants for load-bearing applications, Nat. Commun. 11 (1) (2020) 1–16.

[10] D. Hernández-Escobar, S. Champagne, H. Yilmazer, B. Dikici, C.J. Boehlert, H. Hermawan, Current status and perspectives of zinc-based absorbable alloys for biomedical applications, Acta Biomater. 97 (2019) 1–22.

[11] A. Tripathi, S. Saravanan, S. Pattnaik, A. Moorthi, N.C. Partridge, N. Selvamurugan, Bio-composite scaffolds containing chitosan/nano-hydroxyapatite/nano-copper–zinc for bone tissue engineering, Int. J. Biol. Macromol. 50 (1) (2012) 294–299.

[12] D. Gu, X. Rao, D. Dai, C. Ma, L. Xi, K. Lin, Laser additive manufacturing of carbon nanotubes (CNTs) reinforced aluminum matrix nanocomposites: processing optimization, microstructure evolution and mechanical properties, Additive Manufacturing 29 (2019) 100801.

[13] M. Ali, M. Hussein, N. Al-Aqeeli, Magnesium-based composites and alloys for medical applications: a review of mechanical and corrosion properties, J. Alloys Compd. 792 (2019) 1162–1190.

[14] R. Xu, Z. Tan, G. Fan, J. Gang, Z. Di, High-strength CNT/Al-Zn-Mg-Cu composites with improved ductility achieved by flake powder metallurgy via elemental alloying, Compos. Appl. Sci. Manuf. 111 (2018) 1–11.

[15] S.L. Xiang, M. Gupta, X.J. Wang, L.D. Wang, K. Wu, Enhanced overall strength and ductility of magnesium matrix composites by low content of graphene nanoplatelets, Composites Part A: Applied ence and Manufacturing 100 (2017).

[16] Ke Chu, Fan Wang, Yu-biao Li, Xiao-hu Huang, Da-jian Geng, Interface and mechanical/thermal properties of graphene/copper composite with Mo2C nanoparticles grown on graphene, Composites Part A Applied Science & Manufacturing 109 (2018).

[17] Z. Wu, C. Xu, C. Ma, Z. Liu, H.M. Cheng, W. Ren, Synergistic effect of aligned graphene nanosheets in graphene foam for high-performance thermally conductive composites, Adv. Mater. 31 (19) (2019) 1900199.

[18] R. Guan, Y. Wang, S. Zheng, N. Su, Z. Ji, Z. Liu, Y. An, B. Chen, Fabrication of aluminum matrix composites reinforced with Ni-coated graphene nanosheets, Mater. Sci. Eng. 754 (2019) 437–446.

[19] S.L. Xiang, M. Gupta, X.J. Wang, L.D. Wang, X.S. Hu, K. Wu, Enhanced overall strength and ductility of magnesium matrix composites by low content of graphene nanoplatelets, Compos. Appl. Sci. Manuf. 100 (2017) 183–193.

[20] H. Yue, L. Yao, X. Gao, S. Zhang, E. Guo, H. Zhang, X. Lin, B. Wang, Effect of ball-milling and graphene contents on the mechanical properties and fracture mechanisms of graphene nanosheets reinforced copper matrix composites, J. Alloys Compd. 691 (2017) 755–762.

[21] W. Li, M. Li, J. Liu, Y. Yang, S. Wen, Q. Wei, C. Yan, Y. Shi, Microstructure control and compressive properties of selective laser melted Ti-43.5 Al-6.5 Nb-2Cr-0.5 B alloy: influence of reduced graphene oxide (RGO) reinforcement, Mater. Sci. Eng. 743 (2019) 217–222.

[22] Y. Han, Y. Ke, Y. Shi, Y. Liu, G. Yang, Z. Li, D.-B. Xiong, J. Zou, Q. Guo, Improved mechanical property of nanolaminated graphene (reduced graphene oxide)/Al–Mg–Si composite rendered by facilitated ageing process, Mater. Sci. Eng. (2020) 139541.

[23] A. Raslan, L.S. del Burgo, J. Ciriza, J.L. Pedraz, Graphene oxide and reduced graphene oxide-based scaffolds in regenerative medicine, Int. J. Pharm. (2020) 119226.

[24] M. Amini, S.I. Chang, P. Rao, A cyber manufacturing and AI framework for laser powder bed fusion (LPBF) additive manufacturing process, Manufacturing Letters 21 (2019) 41–44.

[25] H. Qin, V. Fallah, Q. Dong, M. Brochu, M.R. Daymond, M. Gallerneault, Solidification pattern, microstructure and texture development in Laser Powder Bed Fusion (LPBF) of Al10SiMg alloy, Mater. Char. 145 (2018) 29–38.

[26] Y. Qin, P. Wen, D. Xia, H. Guo, M. Voshage, L. Jauer, Y. Zheng, J.H. Schleifenbaum, Y. Tian, Effect of grain structure on the mechanical properties and in vitro corrosion behavior of additively manufactured pure Zn, Additive Manufacturing 33 (2020) 101134.

[27] D. Luo, G. Zhang, J. Liu, X. Sun, Evaluation criteria for reduced graphene oxide, J. Phys. Chem. C 115 (23) (2011) 11327–11335.

[28] A. Shaikh, S. Parida, S. Böhm, One step eco-friendly synthesis of Ag–reduced graphene oxide nanocomposite by phytoreduction for sensitive nitrite determination, RSC Adv. 6 (102) (2016) 100383–100391.

[29] A.A. Dubale, W.-N. Su, A.G. Tamirat, C.-J. Pan, B.A. Aragaw, H.-M. Chen, C.-H. Chen, B.-J. Hwang, The synergetic effect of graphene on Cu 2 O nanowire arrays as a highly efficient hydrogen evolution photocathode in water splitting, J. Mater. Chem. 2 (43) (2014) 18383–18397.

[30] D.A. Dikin, S. Stankovich, E.J. Zimney, R.D. Piner, G.H. Dommett, G. Evmenenko, S.T. Nguyen, R.S Ruoff, Preparation and characterization of graphene oxide paper, Nature 448 (7152) (2007) 457–460.

[31] P. Pokharel, D.S. Lee, Thermal and mechanical properties of reduced graphene oxide/polyurethane nanocomposite, J. Nanosci. Nanotechnol. 14 (8) (2014) 5718–5721.

[32] P. Makvandi, M. Ghomi, M. Ashrafizadeh, A. Tafazoli, T. Agarwal, M. Delfi, J. Akhtari, E.N. Zare, V.V. Padil, A. Zarrabi, A Review on Advances in Graphene-Derivative/polysaccharide Bionanocomposites: Therapeutics, Pharmacogenomics and Toxicity, Carbohydrate Polymers, 2020, p. 116952.

[33] H. Liang, Y. Yang, D. Xie, L. Li, N. Mao, C. Wang, Z. Tian, Q. Jiang, L. Shen, Trabecular-like Ti-6Al-4V scaffolds for orthopedic: fabrication by selective laser melting and in vitro biocompatibility, J. Mater. Sci. Technol. 35 (7) (2019) 1284–1297.

[34] P. Wen, M. Voshage, L. Jauer, Y. Chen, Y. Qin, R. Poprawe, J.H. Schleifenbaum, Laser additive manufacturing of Zn metal parts for biodegradable applications: processing, formation quality and mechanical properties, Mater. Des. 155 (2018) 36–45.

[35] M. Liu, M. Shi, W. Lu, D. Zhu, L. Li, L. Gan, Core–shell reduced graphene oxide/MnOx@ carbon hollow nanospheres for high performance supercapacitor electrodes, Chem. Eng. J. 313 (2017) 518–526.

[36] R. Hu, J. Zhao, J. Zheng, Synthesis of SnO2/rGO hybrid materials by sol-gel/thermal reduction method and its application in electrochemical capacitors, Mater. Lett. 197 (2017) 59–62.

[37] S. Wen, K. Chen, W. Li, Y. Zhou, Q. Wei, Y. Shi, Selective laser melting of reduced graphene oxide/S136 metal matrix composites with tailored microstructures and mechanical properties, Mater. Des. 175 (2019) 107811.

[38] W. Zhang, Y. Yu, X. Zhang, W. Chen, E. Wang, Mechanical anisotropy improvement in ultrafine-grained ZK61 magnesium alloy rods fabricated by cyclic extrusion and compression, Mater. Sci. Eng. 600 (2014) 181–187.

[39] X. Wen, Q. Wang, Q. Mu, N. Kang, S. Sui, H. Yang, X. Lin, W. Huang, Laser solid forming additive manufacturing TiB2 reinforced 2024Al composite: microstructure and mechanical properties, Mater. Sci. Eng. 745 (2019) 319–325.

[40] J.H. Martin, B.D. Yahata, J.M. Hundley, J.A. Mayer, T.A. Schaedler, T.M. Pollock, 3D printing of high-strength aluminium alloys, Nature 549 (7672) (2017) 365–+.

[41] X. Wang, S. Jin, R. Zhang, Y. Liu, J. Wang, Z. Hu, W. Lu, S. Yang, M. Jin, W. Qiao, The influence of dispersion state of graphene sheets on the microstructure and thermal conductivity of free-standing reduced graphene oxide films, Nano 14 (3) (2019) 1950038.

[42] Y. Li, P. Pavanram, J. Zhou, K. Lietaert, P. Taheri, W. Li, H. San, M. Leeflang, J. Mol, H. Jahr, Additively manufactured biodegradable porous zinc, Acta Biomater. 101 (2020) 609–623.

[43] H. Li, X. Xie, Y. Zheng, Y. Cong, F. Zhou, K. Qiu, X. Wang, S. Chen, L. Huang, L. Tian, Development of biodegradable Zn-1X binary alloys with nutrient alloying elements Mg, Ca and Sr, Sci. Rep. 5 (2015) 10719.

[44] E. Mostaed, M. Sikora-Jasinska, A. Mostaed, S. Loffredo, A.G. Demir, B. Previtali, D. Mantovani, R. Beanland, M. Vedani, Novel Zn-based alloys for biodegradable stent applications: design, development and in vitro degradation, Journal of the mechanical behavior of biomedical materials 60 (2016) 581–602.

[45] Y. Qin, P. Wen, H. Guo, D. Xia, Y. Zheng, L. Jauer, R. Poprawe, M. Voshage, J. H. Schleifenbaum, Additive manufacturing of biodegradable metals: current research status and future perspectives, Acta Biomater. 98 (2019) 3–22.

[46] Z. Yanushkevich, S. Dobatkin, A. Belyakov, R. Kaibyshev, Hall-Petch relationship for austenitic stainless steels processed by large strain warm rolling, Acta Mater. 136 (2017) 39–48.

[47] F. Pan, J. Mao, G. Zhang, A. Tang, J. She, Development of high-strength, low-cost wrought Mg–2.0 mass% Zn alloy with high Mn content, Prog. Nat. Sci.: Materials International 26 (6) (2016) 630–635.

[48] L. Li, Z. Zhang, P. Zhang, C. Li, Z. Zhang, Dislocation arrangements within slip bands during fatigue cracking, Mater. Char. 145 (2018) 96–100.

[49] C. Shuai, L. Yu, P. Feng, C. Gao, S. Peng, Interfacial reinforcement in bioceramic/biopolymer composite bone scaffold: the role of coupling agent, Colloids Surf. B Biointerfaces (2020) 111083.

[50] M. Feng, S. Wang, J. Yang, B. Zhang, Core–shell rGO/SnO 2@ CF with wrinkled surface used as structural anode material: high tensile strength and electrochemical stability, J. Mater. Chem. 4 (47) (2016) 18524–18531.

[51] D.-d. Zhang, Z.-j. Zhan, Experimental investigation of interfaces in graphene materials/copper composites from a new perspective, RSC Adv. 6 (57) (2016) 52219–52226.

[52] C. Zhao, J. Wang, Fabrication and tensile properties of graphene/copper composites prepared by electroless plating for structural applications, Phys. Status Solidi 211 (12) (2014) 2878–2885.

[53] L.-C. Tang, Y.-J. Wan, D. Yan, Y.-B. Pei, L. Zhao, Y.-B. Li, L.-B. Wu, J.-X. Jiang, G.-Q. Lai, The effect of graphene dispersion on the mechanical properties of graphene/epoxy composites, Carbon 60 (2013) 16–27.

[54] S. Xu, Z. Zhou, F. Long, H. Jia, N. Guo, Z. Yao, M.R. Daymond, Combination of back stress strengthening and Orowan strengthening in bimodal structured Fe–9Cr–Al ODS steel with high Al addition, Mater. Sci. Eng. 739 (2019) 45–52.

[55] J. Liang, H. Li, L. Qi, W. Tian, X. Li, X. Chao, J. Wei, Fabrication and mechanical properties of CNTs/Mg composites prepared by combining friction stir processing and ultrasonic assisted extrusion, J. Alloys Compd. 728 (2017) 282–288.

[56] R. Askarnia, B. Ghasemi, S.R. Fardi, H.R. Lashgari, E. Adabifiroozjaei, Fabrication of high strength aluminum-graphene oxide (GO) composites using microwave sintering, Adv. Compos. Mater. (2020) 1–15.

[57] R. Jiang, X. Zhou, Q. Fang, Z. Liu, Copper–graphene bulk composites with homogeneous graphene dispersion and enhanced mechanical properties, Mater. Sci. Eng. 654 (2016) 124–130.

[58] K. Chu, F. Wang, Y.-b. Li, X.-h. Wang, D.-j. Huang, Z.-r. Geng, Interface and mechanical/thermal properties of graphene/copper composite with Mo2C nanoparticles grown on graphene, Compos. Appl. Sci. Manuf. 109 (2018) 267–279.

[59] J. Bhattacharyya, F. Wang, N. Stanford, S. Agnew, Slip mode dependency of dislocation shearing and looping of precipitates in Mg alloy WE43, Acta Mater. 146 (2018) 55–62.

[60] S.W. Lee, S.-H. Kim, W.-K. Jo, W.-H. Hong, W. Kim, B.G. Moon, S.H. Park, Twinning and slip behaviors and microstructural evolutions of extruded Mg-1Gd alloy with rare-earth texture during tensile deformation, J. Alloys Compd. 791 (2019) 700–710.

[61] H. Bakhsheshi-Rad, E. Hamzah, H. Low, M. Kasiri-Asgarani, S. Farahany, E. Akbari, M. Cho, Fabrication of biodegradable Zn-Al-Mg alloy: mechanical properties, corrosion behavior, cytotoxicity and antibacterial activities, Mater. Sci. Eng. C 73 (2017) 215–219.

[62] A. Kafri, S. Ovadia, G. Yosafovich-Doitch, E. Aghion, In vivo performances of pure Zn and Zn–Fe alloy as biodegradable implants, J. Mater. Sci. Mater. Med. 29 (7) (2018) 94.

[63] X. Liu, J. Sun, F. Zhou, Y. Yang, R. Chang, K. Qiu, Z. Pu, L. Li, Y. Zheng, Micro-alloying with Mn in Zn–Mg alloy for future biodegradable metals application, Mater. Des. 94 (2016) 95–104.

[64] S. Zhao, C.T. McNamara, P.K. Bowen, N. Verhun, J.P. Braykovich, J. Goldman, J. W. Drelich, Structural characteristics and in vitro biodegradation of a novel Zn-Li alloy prepared by induction melting and hot rolling, Metall. Mater. Trans. 48 (3) (2017) 1204–1215.

[65] J. Cheng, Y. Zheng, In vitro study on newly designed biodegradable Fe-X composites (X= W, CNT) prepared by spark plasma sintering, J. Biomed. Mater. Res. B Appl. Biomater. 101 (4) (2013) 485–497.

[66] Y. Yang, X. Guo, C. He, C. Gao, C. Shuai, Regulating degradation behavior by incorporating mesoporous silica for Mg bone implants, ACS Biomater. Sci. Eng. 4 (3) (2018) 1046–1054.

[67] H. Yang, X. Qu, W. Lin, D. Chen, D. Zhu, K. Dai, Y. Zheng, Enhanced osseointegration of Zn-Mg composites by tuning the release of Zn ions with sacrificial Mg-rich anode design, ACS Biomater. Sci. Eng. 5 (2) (2018) 453–467.

[68] R. Patil, P. Bahadur, S. Tiwari, Dispersed graphene materials of biomedical interest and their toxicological consequences, Adv. Colloid Interface Sci. 275 (2020) 102051.

[69] B. Zhang, P. Wei, Z. Zhou, T. Wei, Interactions of graphene with mammalian cells: molecular mechanisms and biomedical insights, Adv. Drug Deliv. Rev. 105 (2016) 145–162.

[70] C. Shuai, G. Liu, Y. Yang, F. Qi, S. Peng, W. Yang, C. He, G. Wang, G. Qian, A strawberry-like Ag-decorated barium titanate enhances piezoelectric and antibacterial activities of polymer scaffold, Nanomater. Energy (2020) 104825.

[71] C. Shuai, W. Yang, P. Feng, S. Peng, H. Pan, Accelerated degradation of HAP/PLLA bone scaffold by PGA blending facilitates bioactivity and osteoconductivity, Bioactive Materials 6(2) 490-502.

[72] P. Feng, S. Peng, C. Shuai, C. Gao, W. Yang, S. Bin, A. Min, In situ generation of hydroxyapatite on biopolymer particles for fabrication of bone scaffolds owning bioactivity, ACS Applied Materials & Interfaces 12 (2020).

[73] W. Yang, Y. Zhong, C. He, S. Peng, Y. Yang, F. Qi, P. Feng, C. Shuai, Electrostatic self-assembly of pFe3O4 nanoparticles on graphene oxide: a co-dispersed nanosystem reinforces PLLA scaffolds, J. Adv. Res. 24 (2020).

[74] X. Zou, L. Zhang, Z. Wang, Y. Luo, Mechanisms of the antimicrobial activities of graphene materials, J. Am. Chem. Soc. 138 (7) (2016) 2064–2077.

[75] L. Cao, W. Liu, Y. Zhong, Y. Zhang, D. Gao, T. He, Y. Liu, Z. Zou, Y. Mo, S. Peng, Linc 02349 promotes osteogenesis of human umbilical cord-derived stem cells by acting as a competing endogenous RNA for miR-25-3p and miR-33b-5p, Cell Prolif 53 (5) (2020), e12814.